Journal of Sol-Gel Science and Technology (2024) 111:553–565
https://doi.org/10.1007/s10971-024-06471-0

ORIGINAL PAPER

Visible light-driven removal of Rhodamine B using indium-doped zinc oxide prepared by sol–gel method

Majdi Benamara[1] · Kais Iben Nassar[2] · Manel Essid[3] · Stefanie Frick[4] · R. Rugmini[5] · K. C. Sekhar[5] · José P. B. Silva[6,7]

Received: 24 April 2024 / Accepted: 27 June 2024 / Published online: 10 July 2024
© The Author(s) 2024

Abstract

Industrial dye contamination in wastewater poses significant environmental challenges, necessitating the development of efficient photocatalysts for degradation. In this work, we investigate the In doping effect in the photocatalytic activity of zinc oxide (ZnO) nanoparticles for effective RhB degradation. Indium-doped ZnO nanoparticles were synthesized via sol–gel method and x-ray diffraction (XRD) analysis revealed a wurtzite hexagonal structure, with the crystallite size being varying from 65 nm to 53 nm with the introduction of In content. XPS measurements on the 3% In-doped ZnO sample revealed distinct core level spectra for In 3d, Zn 2p, and O 1s regions, confirming the presence of indium, zinc, and oxygen. Brunauer–Emmett–Teller (BET) analysis revealed increased surface area and pore size, with specific surface areas escalating from 0.9 m²/g for pure ZnO to 10.1 m²/g for 3% indium-doped ZnO. Photocatalytic experiments exhibited significant RhB degradation, with degradation efficiencies reaching 93% for 3% indium-doped ZnO under visible light irradiation due to the effect of the presence of In, which causing light absorption enhancement, narrow the band gap and improve charge carrier separation. These findings underscore the potential of indium-doped ZnO nanoparticles as efficient and sustainable photocatalysts for wastewater treatment, offering a promising avenue to address environmental challenges associated with industrial dye-contaminated effluents.

Graphical Abstract

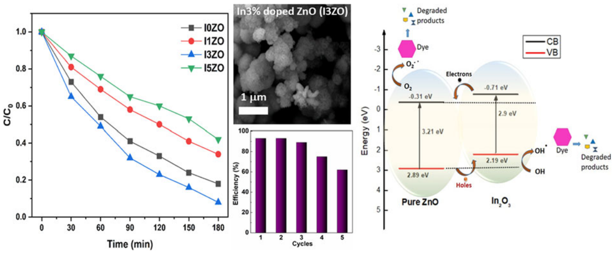

Keywords Indium doping · Nanoparticle characterization · Photocatalysis · Rhodamine B degradation · Wastewater treatment · Zinc oxide

---

✉ Majdi Benamara
majdibenamara1@gmail.com

✉ José P. B. Silva
josesilva@fisica.uminho.pt

[1] Laboratory for Building Energy Materials and Components, Swiss Federal Laboratories for Materials Science and Technology (Empa), Dübendorf, Switzerland

[2] Department of Chemistry, CICECO—Aveiro Institute of Materials, University of Aveiro, Aveiro, Portugal

[3] Chemistry Department, College of Science, King Khaled University (KKU), Abha 61413, P.O. Box 9004, Saudi Arabia

[4] Laboratory for Surface Science and Coating Technologies, Swiss Federal Laboratories for Materials Science and Technology (Empa), Dübendorf, Switzerland

[5] Department of Physics, Central University of Tamil Nadu, Thiruvarur, India

[6] Physics Center of Minho and Porto Universities (CF-UM-UP), University of Minho, Campus de Gualtar, Braga, Portugal

[7] Laboratory of Physics for Materials and Emergent Technologies, LapMET, University of Minho, Braga, Portugal

Highlights

- Sol–gel synthesis of Indium-doped ZnO offers a scalable method for effective photocatalysts in wastewater treatment.
- Achieved 93% Rhodamine B degradation with Indium-doped ZnO nanoparticles under visible light.
- XRD analysis showed a reduction in crystallite size from 65 nm (pure ZnO) to 53 nm (3% In-doped ZnO).
- BET surface area increased from 0.9 m²/g (pure ZnO) to 10.1 m²/g (3% In-doped ZnO).
- UV-Vis spectroscopy indicated a reduced band gap in Indium doped ZnO (3.19 eV).
- TGA analysis highlighted improved thermal stability in Indium doped ZnO nanoparticles.

1 Introduction

The treatment of wastewater generated from industrial processes is imperative to mitigate its adverse impact on the environment, living organisms, and human health [1, 2]. This concern is particularly pronounced in industries such as textiles, paper, cosmetics, and printing, where xanthene dyes are extensively utilized [3, 4]. These dyes, including Rhodamine B (RhB), pose significant environmental hazards due to their water solubility and carcinogenic nature. When discharged into water bodies, these dyes can disrupt aquatic ecosystems and endanger human health through bioaccumulation in the food chain. Various techniques have been employed for wastewater treatment, ranging from conventional methods like sedimentation and filtration to advanced processes such as chemical oxidation and biological treatment [5]. Among these, Advanced Oxidation Processes (AOPs), particularly heterogeneous photocatalysis, have emerged as promising methods for degrading organic pollutants under UV/Vis light [6]. This process involves the generation of highly reactive hydroxyl radicals (OH) that can effectively oxidize organic contaminants, transforming them into harmless byproducts like water and carbon dioxide [7].

Zinc oxide (ZnO), known for its wide band gap and high quantum efficiency, has gained attention for its photocatalytic applications. However, despite its intrinsic photocatalytic properties, ZnO suffers from limitations such as rapid charge carrier recombination, which reduces its overall efficiency [8]. To address this challenge, efforts have focused on enhancing ZnO's efficacy through various means, including metal ion doping, surface modification, and nanostructuring. Metal ion doping, in particular, has shown promise in improving ZnO's photocatalytic performance by modifying its electronic band structure and reducing charge carrier recombination rates [9, 10].

In recent years, visible-light-driven photocatalysts have garnered attention for their eco-friendly potential. Unlike traditional photocatalysts, which are primarily activated by UV light, visible-light-driven photocatalysts can harness solar energy more efficiently, making them cost-effective and sustainable alternatives for wastewater treatment [11, 12]. Various strategies, including transition metal-ion doping, rare earth metal doping, co-doping, polymer modification, hetero-junction formation, and dye sensitization, have been explored to activate photocatalysts under visible light [13, 14]. Dye sensitization, in particular, offers a promising approach for enhancing the photocatalytic activity of semiconductor materials by harnessing the light-absorbing properties of organic dyes [15].

Dye sensitization involves the continuous adsorption of dye molecules on the semiconductor surface, followed by their degradation upon excitation by visible light. This process facilitates electron transfer from the dye molecules to the semiconductor, initiating the photocatalytic reaction for organic pollutant degradation [16, 17]. Moreover, dye sensitization can extend the absorption range of photocatalysts into the visible region of the electromagnetic spectrum, enabling more efficient utilization of solar energy for wastewater treatment. Thus, the integration of dye sensitization with photocatalysis holds significant potential for developing sustainable and effective solutions for addressing environmental challenges associated with industrial wastewater containing xanthene dyes [18, 19].

Ways to further enhance the photodegradation properties of pollutants in water have been explored by many researchers who have used doping with alkaline-earth, transition, and post-transition metal elements. For instance, doping ZnO with Ca, was studied by Alejandro et al. [20] and it was demonstrated that it enhances the removal of tetracyclines (10 ppm) by sonophotocatalysis under visible light, achieving over 99% mineralization in 90 min for Ca-doped ZnO at 2%. Benamara et al. [21] revealed that Al doping enhances the removal of cyanotoxins in ZnO nanoparticles with visible LED irradiation. Ersöz et al. [22] showed that doping ZnO with Ag, a post-transition metal element, enhances the removal of RhB, achieving ~66% decomposition after 120 min under UV light irradiation. Doping ZnO with post-transition metal elements enhances photocatalytic dye removal via bandgap narrowing, reduced electron-hole recombination, improved charge separation, increased surface area, and synergistic effects, enhancing efficiency in degrading organic pollutants like RhB [23, 24]. In this study, we explored In as a dopant in ZnO nanoparticles. Indium doping was chosen because of its ability to introduce intermediate energy levels within the ZnO bandgap and improve charge separation efficiency during photocatalysis. Therefore, we have investigated the photo-degradation of RhB by using different indium doping content in ZnO nanoparticles.

2 Experimental details

2.1 Nanoparticles preparation

Indium doped zinc oxide (IZO) nanoparticles were synthesized via the sol–gel method, utilizing 16 g of zinc acetate dehydrate [$Zn(CH_3COO)_2{\cdot}2H_2O$; 99%] as the precursor in 112 mL of methanol. The synthesis process involved magnetic stirring at room temperature for 10 min. Subsequently, the appropriate quantity of indium chloride ($InCl_3$) was added to achieve [In]/[Zn] ratios of 0.01, 0.03, and 0.05. After an additional 15 min of magnetic stirring, the solution was transferred to an autoclave and subjected to drying under supercritical conditions of ethyl alcohol (EtOH). The resulting nanopowders were then subjected to heat treatment in a furnace at 400 °C for 2 h in an air environment. The synthesized samples were assigned unique codes based on the nominal indium loading of each sample: I0ZO, I1ZO, I3ZO, and I5ZO.

2.2 Characterization

The following analytical techniques were employed for comprehensive characterization: Thermogravimetric Analysis (TGA) spectroscopy, X-ray Diffraction (XRD), Scanning Electron Microscopy (SEM) coupled with Energy-Dispersive X-ray Spectroscopy (EDX), Fourier-Transform Infrared (FTIR) spectroscopy, Brunauer–Emmett–Teller (BET) measurement, and Photoluminescence (PL) measurements. These methods collectively provide precise information about crystal structure, surface morphology, particle size, chemical element compositions, surface area, pore sizes, and more.

The X-ray diffraction patterns were captured within the 2θ range spanning from 20° to 70°, utilizing a Bruker Philips X-Pert diffractometer with Ni β-filtered Cu-Kα radiation (1.54178 Å radiation). The average crystallite size (d) was determined using Scherrer's [25–27]

$$d = \frac{0.9\lambda}{B\cos\theta_B} \tag{1}$$

Where λ represents the X-ray wavelength, θ_B is the maximum of the Bragg diffraction peak (in radians), and B is the full width at half maximum (FWHM) of the (101) XRD peak.

Surface images of the samples were obtained using an FEI Inspect S instrument, coupled with an Oxford INCA PentaFETx3 EDX spectrometer. The instrument featured a resolution of 137 eV at 5.9 keV (Mn $K\alpha_1$) and was equipped with a nitrogen-cooled Si(Li) detector. Spectral data were collected at a working distance of 10 mm, an acceleration voltage of 20 kV, counting times of 60 s, and an approximate count rate of 3000 counts/s (cp).

BET measurements were conducted using N_2-physisorption at 77 K with a pressure transducer. Prior to the N_2 physisorption analyses, the samples underwent degassing at 150 °C for 12 h under a flow of N_2.

Photoluminescence (PL) measurements were performed on a NanoLog modular spectrofluorometer Horiba, employing a Xe lamp as the excitation light source at room temperature. Excitation occurred at a wavelength of 325 nm, and emissions were recorded between 350 and 750 nm. The optical absorbance spectra were measured using a Shimadzu UV-3101 PC UV-Vis-NIR spectrophotometer, covering a wavelength range of 200 nm to 800 nm.

X-ray photoelectron spectroscopy (XPS) measurements were performed for the I3ZO sample on a PHI Quantum 2000. Prior to the measurement, the nanopowder was fixed on adhesive carbon tape. The excitation energy was 1486.7 eV (monochromatic Al $K\alpha_1$), while operating the X-ray source at a power of 50 W and a voltage of 15 kV. The pressure during the measurement was on the order of $\sim 2\times10^{-9}$ Torr. A dual beam (electron and ion) neutralizer was used for charge compensation. Charge referencing was performed by aligning the C1s emission line from the carbon tape to 284.5 eV corresponding to the C 1 s core level binding energy of graphite [28]. The In/Zn ratio was calculated from the In $3d_{5/2}$ and Zn $2p_{3/2}$ peaks after Shirley background subtraction and applying the appropriate corrected sensitivity factors.

2.3 Photocatalysis experiment

100 mL of 0.2 μM RhB dye solution was prepared and kept in the dark to avoid any disturbance before applying the catalyst. 20 mg of catalyst was then mixed with dye solution in the dark and kept for some time to attain the equilibrium. This mixture was irradiated by visible light using Heber photoreactor. At each 30 min interval of irradiation, the absorption spectrum was recorded to analyze the RhB degradation. To check the stability of the sample the same procedure was repeated by recovering the used catalyst each time and adding it to fresh dye solution for phototdegradation.

3 Results and discussion

3.1 SEM and EDS analysis of in-doped ZnO

The morphology of In-doped ZnO samples, annealed at 400 °C for 2 h, was examined through scanning electron microscopy (SEM). Figure 1a–c depict SEM images corresponding to I1ZO, I3ZO, and I5ZO, respectively. The SEM analysis reveals the presence of round agglomerates with dimensions ranging between 1 and 5 μm, exhibiting

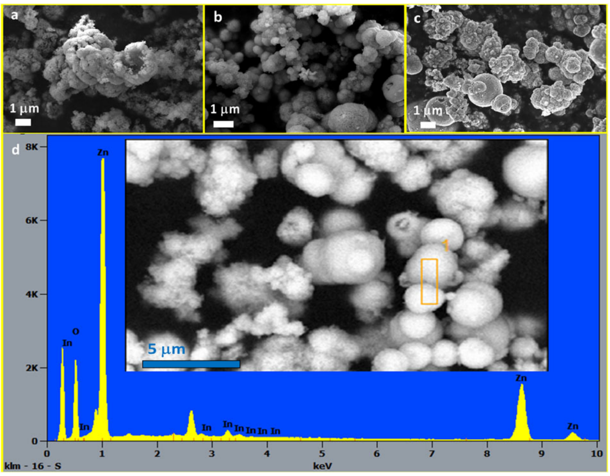

Fig. 1 SEM images of (**a**) I1ZO, (**b**) I3ZO, and (**c**) I5ZO samples (scale 1 µm). **d** EDS spectrum of I5ZO sample

spherical shapes and featuring a rough, porous, fine-grained microstructure. It was observed that the average smallest agglomerate was achieved for sample I3ZO.

To further ascertain the elemental composition within the In-doped ZnO structure, energy-dispersive X-ray spectroscopy (EDS) measurements were performed on the I5ZO sample, as illustrated in Fig. 1d. The EDS analysis indicates a significant presence of oxygen and zinc elements, with a relatively lower concentration of indium elements. This observation underscores the essential elements required for our structural composition, emphasizing the incorporation of indium into the ZnO matrix.

3.2 Microstructural analysis of annealed In-doped ZnO samples

The microstructure of the annealed In-doped ZnO (IZO) samples was examined through X-ray diffraction (XRD), and the obtained spectra are presented in Fig. 2. The discerned peaks were unequivocally indexed to the wurtzite hexagonal-shaped ZnO with the space group P63mc, in accordance with the Joint Committee on Powder Diffraction Standards (JCPDS) card file no 01-073-8765 [29]. These peaks correspond to the (100), (002), (101), (102), (110), and (103) planes of ZnO [30, 31]. At higher dopant concentrations (I3ZO and I5ZO samples) two additional peaks, attributed to a secondary phase, correspond to the (222) and (440) planes of the cubic bixbyite crystal structure of In_2O_3, within the space group Ia-3 (JCPDS card file 06-0416) [32].

The calculated lattice parameters, derived from the (100) and (002) planes, closely align with typical wurtzite ZnO values [33], yielding $a = 3.251$ Å and $c = 5.203$ Å. Utilizing the Scherrer equation, the average crystallite size (d) was estimated from the full width at half maximum (FWHM) of the diffraction peak. For the pure ZnO, the average crystallite size was 65 nm, while for I1ZO, I3ZO, and I5ZO samples, sizes of 53 nm, 56 nm, and 54 nm, respectively, were determined. These results provide valuable insights into the microstructural evolution induced by indium doping in ZnO.

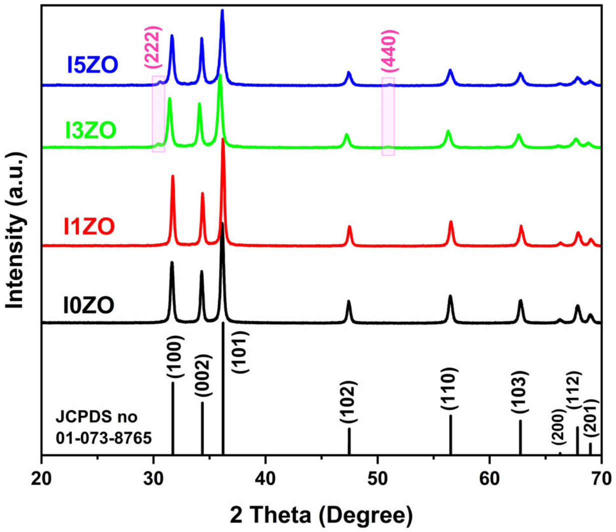

Fig. 2 XRD patterns of I0ZO, I1ZO, I3ZO and I5ZO samples

3.3 Room-temperature photoluminescence analysis

Figure 3 presents the room-temperature photoluminescence (PL) spectrum captured across the 350–800 nm range for both pure and In-doped ZnO samples. From Fig. 3, it can be observed that, the pure ZnO sample exhibit a sharp and less intense emission peak at 390 nm which correspond to the near band edge (NBE) peak responsible for the recombination of free excitons within ZnO [34] and a broad and high intense emission peak at around 540 nm which correspond to the deep level emission (DLE) responsible for transitions within the bandgap. The substantial increase in the NBE peak intensity for the In-doped ZnO sample is due to improved crystalline quality and reduced defect concentration from In doping. In^{3+} ions minimize structural defects, resulting in a more ordered crystal structure and higher radiative recombination probability [35, 36]. Additionally, In^{3+} ions introduce shallow donor levels, increasing the concentration of free carriers that enhance NBE emission. This combination of reduced defects and increased free carriers leads to the observed increase in NBE peak intensity [37]. These defects create localized electronic states within the bandgap, which can trap and recombine charge carriers generated by photoexcitation. The intensity of the DLE peak appears least for I3ZO as shown in Fig. 3. This decrease can be attributed to In^{3+} ions reducing the concentration of oxygen defects responsible

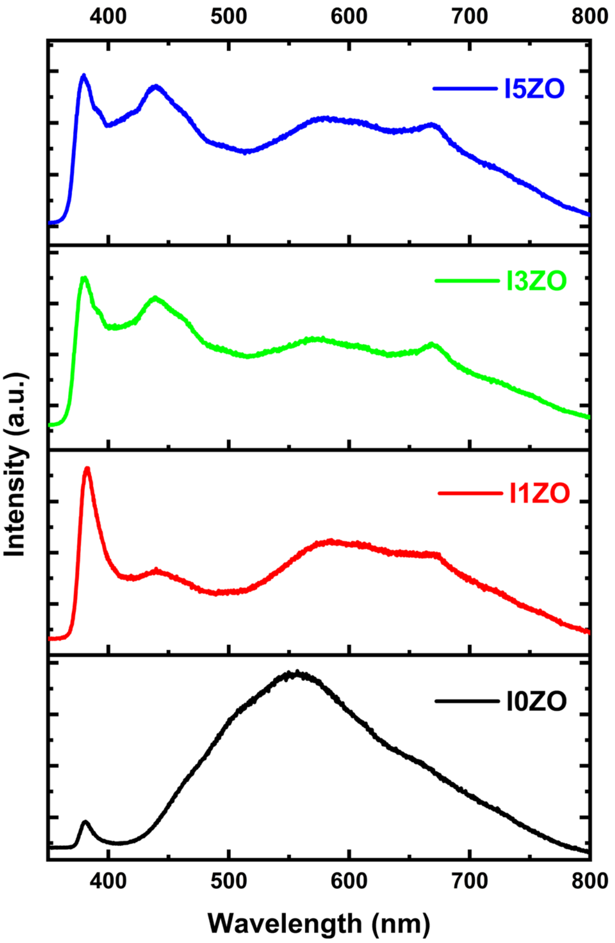

Fig. 3 PL spectra of IZO samples annealed at 400 °C for 2 h in air

for this emission peak by occupying lattice sites otherwise available for defect formation [38]. As acceptor dopants, In^{3+} ions help maintain charge neutrality, decreasing the need for oxygen vacancies. Additionally, In doping enhances ZnO's crystalline quality by minimizing structural defects, resulting in a more ordered crystal structure. Experimental studies show that In-doped ZnO has fewer oxygen vacancies compared to undoped ZnO due to In^{3+} ions during growth or annealing [39, 40].

3.4 UV-Visible absorbance spectra of the prepared IZO samples

To explore the optical characteristics and band gap, absorbance spectra of the samples were assessed using a UV-Vis spectrophotometer. The absorption spectra of pure and 3% In-doped ZnO nanoparticles in the UV and visible ranges are depicted in the Fig. 4. The spectra indicate pronounced absorption in the UV range (200–380 nm) and comparatively lower absorption in the visible range. Notably, absorbance varies with increasing doping concentration in the visible range. Utilizing a classical Tauc approach, the band gap (E_g) of the synthesized samples was determined [41]. The doped ZnO sample exhibited a slightly reduced gap energy (3.19 eV) compared to pure ZnO (3.21 eV), likely due to disorder induced by defects in the ZnO matrix. Furthermore, the band gap energy decreased slightly with rising indium concentration. The diminished band gap energy of In-doped ZnO nanoparticles holds promise for enhancing their photocatalytic activity, particularly in RhB photodegradation. A smaller band gap facilitates better utilization of visible light, leading to increased electron-hole pair generation and subsequent formation of reactive oxygen species responsible for organic pollutant degradation. Additionally, indium dopants introduce defect states within the band gap, serving as trapping sites for photogenerated charge carriers, thereby prolonging their lifetime and enhancing photocatalytic efficiency [42].

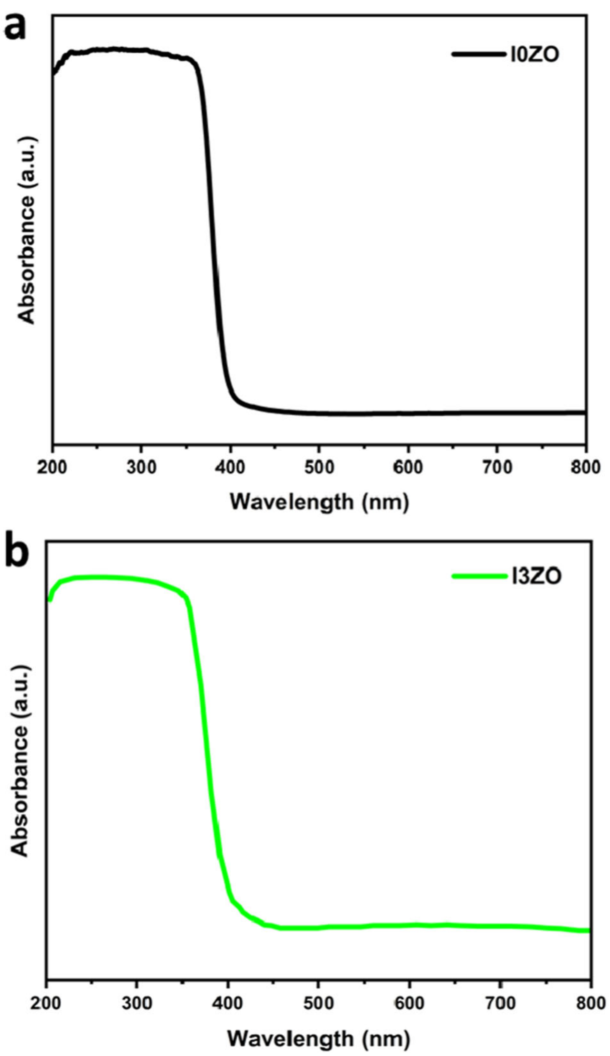

Fig. 4 Absorbance spectra of (**a**) I0ZO, and (**b**) I3ZO

3.5 Fourier transform Infrared spectroscopy (FTIR) spectra of IZO NPs

The FTIR spectra in Fig. 5 depict a comparison between pure ZnO nanoparticles and those incorporating indium doping. Across all spectra, a consistent broadband is observed, centered at 3415 cm^{-1}, indicating O–H stretching [43]. Additionally, the band within the 866–875 cm^{-1} range is associated with C–H bending, and the band at 695–673 cm^{-1} is attributed to M−O−M (M = Zn, In) interactions. The introduction of In results in the emergence of two new bands at 1525 and 1357 cm^{-1}, suggesting the formation of carbonate species [44].

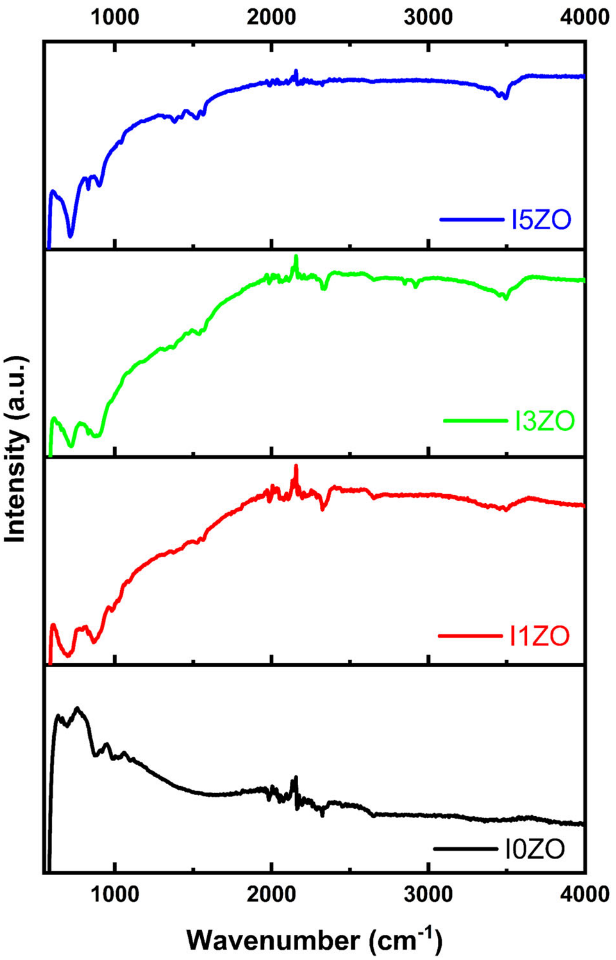

Fig. 5 FTIR spectra of pure and In-doped ZnO

3.6 X-ray photoelectron spectroscopy (XPS) on In-doped ZnO

For the 3% In-doped ZnO sample, XPS measurements were performed. The corresponding core level spectra of the In 3d, Zn 2p, and O 1s regions are displayed in Fig. 6. An intense C 1s signal from the graphitic substrate (carbon tape) was observed, shown in Fig. S1 (see supporting information). The In 3d and Zn 2p core levels show both a doublet occurring due to spin-orbit-coupling, while the two peaks visible in the O 1s spectrum are attributed to two different oxygen species. The relative intensity of the high binding energy component in the O 1s spectra is increasing for lower substrate coverage with the I3ZO powder and still present for the bare substrate. Therefore, the high binding energy component in the O 1s spectra can be assigned to a substrate-related oxygen species, rather than to an often discussed different core hole screening state [45, 46]. The low binding energy component lays well in the region of reported O 1s peak positions for ZnO (540.4 ± 0.5 eV [47], 540.4 [48]) and In_2O_3 (540.5 ± 0.5 eV [47]). Considering the In 3d spectrum, the binding energy of both doublet peaks are in line with the mean value calculated from the NIST XPS database for In_2O_3 (In $3d_{5/2}$: 444.8 ± 0.6 eV) [47]. Other In(III) chalcogenides and pnictogens as well as some In(I) halide compounds show similar In 3d line positions [48], while the respective values of the metallic In(0) are reported roughly 1 eV lower (443.8 ± 0.3 eV [47]). In case of the Zn 2p, the binding energy agree with the

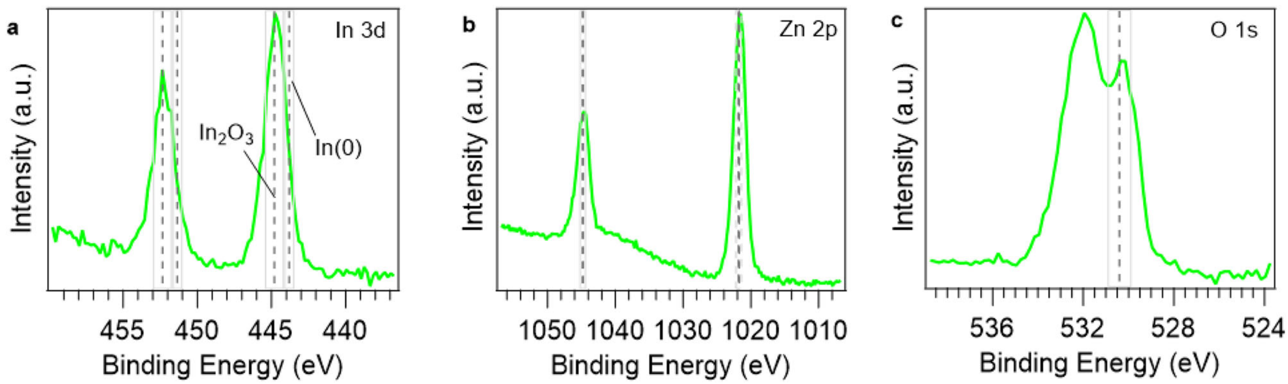

Fig. 6 XPS core level spectra of the (**a**) In 3d, (**b**) Zn 2p, and (**c**) O 1s regions. The dashed lines and gray regions are mean values and the respective standard deviation of the binding energies reported in the NIST database [47]. In case of the Zn 2p peaks, the regions of metal and oxide are overlapping. The O 1s reference values are based on the reported values for ZnO

ranges of both Zn(II) in ZnO and metallic Zn(0) from literature (Zn $2p_{3/2}$: 1021.8 ± 0.4 eV and 1021.7 ± 0.3 eV [46]). Therefore, an unambiguous differentiation of Zn oxidation states from the binding energy alone is difficult. While chemical state analysis based on the Zn 2p core level emission is often ambiguous, the Zn LMM Auger emission exhibits much more pronounced chemical shifts [49]. When considering the Zn LMM Auger line (see supporting information), its position relative to the Zn $2p_{3/2}$ matches with Zn(II) rather than with the one for Zn(0) [50]. To conclude, for both In and Zn, there are no indications for metallic species but both elements show typical spectra expected for ZnO and In_2O_3. Addressing the indication of carbonate species from the FTIR, a second, low intensity peak in the C 1s spectrum is present at ~4 eV higher binding energies than the graphitic peak, which could be attributed to carbonates (O-C=O species: 3.8–4.3 eV higher [45]). Since a similar peak is also observed in the spectrum of the bare substrate, a final assignment to a powder related carbonate cannot be made with certainty. From the In $3d_{5/2}$ and Zn $2p_{3/2}$ peaks, a In/Zn ratio of 0.08 ± 0.01 was obtained for the I3ZO sample.

3.7 BET spectra of IZO nanoparticles

Figure 7 displays the Brunauer-Emmet-Teller (BET) adsorption-desorption isotherms for pure ZnO and $In_{3\%}$-doped ZnO samples synthesized through the sol–gel method. As per IUPAC classification, the registered isotherms exhibit type II characteristics. The presence of In3% doping results in clustered particles with a mesoporous architecture and an unrestricted monolayer-multilayer adsorption, as evidenced by an H_3-type hysteresis loop [51]. The incorporation of In leads to a substantial increase in the surface areas of the ZnO nanoparticles compared to the pure ZnO counterparts. Specifically, the projected specific surface area (S_{BET}) experiences a nearly 10 fold increase, escalating from 0.9 $m^2\,g^{-1}$ for pure ZnO to 10.1 $m^2\,g^{-1}$ for the 3 percent In-doped sample. The insets in Fig. 7a, b depict the Barret-Joyner-Halenda (BJH) pore size distribution for I0ZO and I3ZO samples, respectively. All pore sizes fall within the mesoporous range, with average diameters less than 50 nm, consistent with typical mesoporous material characteristics. A noteworthy augmentation in the average pore diameter is observed, progressing from 7.4 nm for pure ZnO to 36.9 nm for the $In_{3\%}$-doped ZnO samples.

3.8 Thermogravimetric (TG) analysis

Thermogravimetric analysis (TGA) was employed to assess the thermal stability of ZnO and In3%-doped ZnO nanoparticles (NPs) by monitoring the weight loss of volatile components in the arranged samples. Figure 8 presents the TGA thermograms for I0ZO and I3ZO NPs. The distinct TGA regions with percentage weight loss are depicted in Fig. 8.

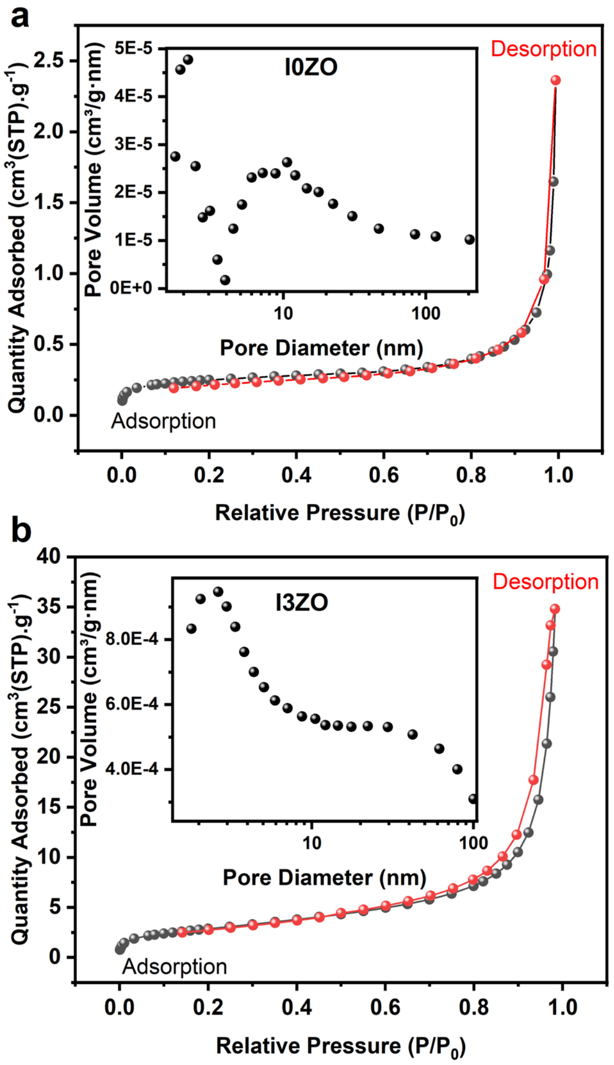

Fig. 7 Nitrogen adsorption-desorption isotherms with pore size distribution (inset) of (**a**) the pure ZnO and (**b**) the $In_{3\%}$ doped ZnO

In Fig. 8a, the initial region of ZnO NPs, observed up to 200 °C, exhibited a weight loss of ~1.3% attributed to moisture evaporation and the disintegration of volatile organic compounds. This observation was further confirmed by the peak intensity of the derivative thermogravimetric (DTG) curve at 99.9 °C. Similarly, in Fig. 8b, the first region of the TGA curve for I3ZO NPs, up to 200 °C, with a DTG intensity at 173.2 °C, was linked to the evaporation of surface moisture on I3ZO NPs, resulting in a weight loss of about 1.5%.

The TGA region between 200–800 °C for pure ZnO NPs exhibited sharp peaks in the DTG curve at 208 °C, 286.6 °C, and 425.5 °C. These peaks were associated with the thermal decomposition of volatile functional groups from various phytochemicals acting as reducing or stabilizing agents in the biogenesis of ZnO NPs, leading to a

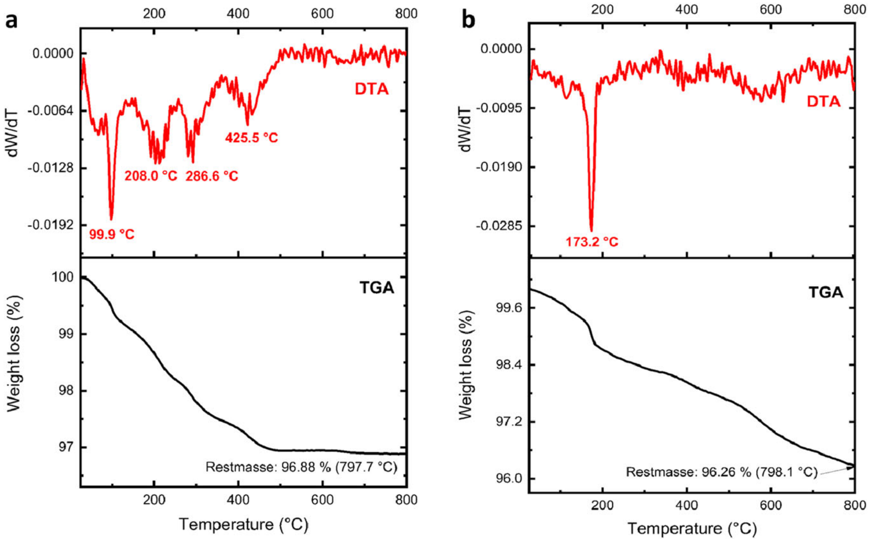

Fig. 8 Thermogravimetric (TG) analysis with TDA curves of (**a**) the I0ZO and the (**b**) I3ZO samples

weight loss of 1.82%. In contrast, for the I3ZO sample, a weight loss of 2.24% was observed in the TGA curve between 200–800 °C.

The weight loss observed between 200–500 °C in the TGA curve for both samples was attributed to the decomposition of lower molecular weight phytochemicals [52]. Additionally, in the TGA curve region between 500–800 °C, it is believed that the weight loss resulted from the thermal decomposition of higher molecular weight phytochemicals serving as capping or stabilizing agents [53]. In addition, the presence of carbon in the structure of In-doped ZnO nanoparticles (I3ZO NPs) compared to pure ZnO nanoparticles (I0ZO NPs) can be attributed to the higher weight loss observed in the TGA analysis for I3ZO NPs. The TGA results indicate that I3ZO NPs exhibit a higher weight loss (3.74%) compared to I0ZO NPs (3.12%), suggesting a greater presence of organic carbon components in the In-doped sample [54]. The presence of these organic carbon components can potentially influence the photocatalytic activity of the nanoparticles, including the photodegradation of RhB. Carbon-based materials are known to enhance the photocatalytic performance of semiconductors like ZnO by acting as sensitizers, facilitating charge separation, and promoting the formation of reactive oxygen species [55]. However, the specific effect of the carbon components present in the In-doped ZnO nanoparticles on the photodegradation of RhB requires further investigation.

3.9 RhB degradation by In doped ZnO photocatalysts

The absorbance spectra of the RhB solutions containing I0ZO, I1ZO, I3ZO, and I5ZO are presented in the Fig. 9a–d, respectively. The decrease in dye concentration was detected with the increase in time, and ultimately, the dye was degraded after 180 min. It is due to the fact that the nanoparticles acted as catalysts to degrade the dye molecules. These results of RhB degradation have shown 82% degradation by using pure zinc oxide nanoparticles as represented in Fig. 10a. After the doping of ZnO with In, the degradation of dye was found to be increased by 93%, which is much higher than undoped nanoparticles, particularly for the sample I3ZO.

The concentration report C/C_0 is crucial for understanding the reaction kinetics. It can be depicted through the equation: Ln $(A_t/A_0) = -kt$ [56, 57], here, k stands for the pseudo-first-order rate constant, t denotes the reaction time, A_0 represents the initial concentration of RhB at $t = 0$, and A_t signifies the concentration at time t, which can be derived from the absorbance of the peak at 550 nm. The constant k can be accurately determined directly from the slope of the straight line resulting from plots of ln (A_t/A_0) versus reaction time, presented in Fig. 10b. The values of k for I0ZO, I1ZO, I3ZO, and I5ZO were 9.36×10^{-3}, 5.86×10^{-3}, 13.26×10^{-3}, and 4.56×10^{-3} min^{-1}, respectively. The value of k indicates how fast the dye degradation reaction proceeds. A higher value of k implies a faster rate of reaction, and hence it is clear that I3ZO is more efficient in facilitating the degradation of the dye molecule. This can be attributed to the large specific surface area and pore diameter of the I3ZO catalyst as evident from BET studies. The large surface area provides more active sites allow for more reactant molecules to come into contact with the catalyst surface, leading to enhanced catalytic activity and the large pore diameter facilitates the diffusion of reactant molecules to and from the active sites within the catalyst structure enhancing the reaction kinetics. In addition to that, the reduced recombination rate of charge carriers in the presence of I3ZO as evident from PL studies also contributes to the high efficiency of I3ZO catalyst.

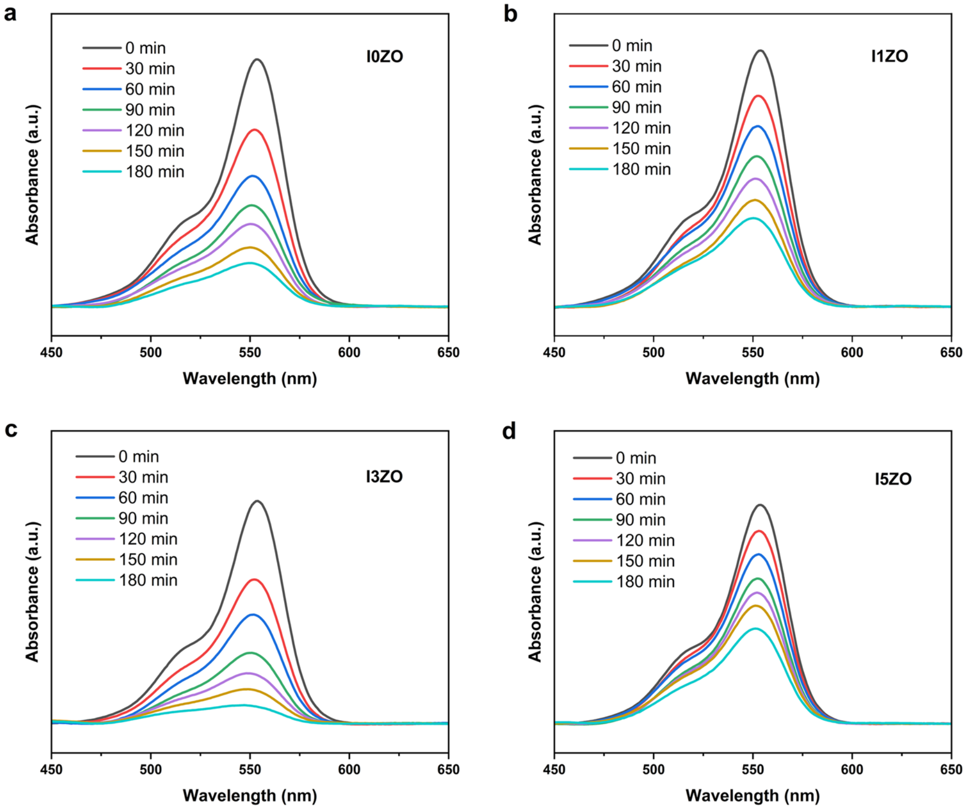

Fig. 9 Visible Absorbance Spectra Illustrating the Degradation of RhB Dye in the Presence of (**a**) I0ZO, (**b**) I1ZO, (**c**) I3ZO, and (**d**) I5ZO Catalysts

A schematic diagram of the underlying mechanism of the photocatalytic degradation is shown in Fig. 11. The valence band (VB) and conduction band (CB) values are calculated from Mulliken electronegativity approach. Under visible light irradiation, the photocatalysts become excited, generating electrons and holes.

$$ZnO + h\vartheta \rightarrow e^-_{CB} + h^+_{VB} \quad (2)$$

Since the CB edge potential of In_2O_3 is more negative than that of ZnO, the electrons from In_2O_3 can easily transfer to the CB of ZnO [58]. This transfer facilitates the efficient separation of photogenerated electron-hole pairs, reducing recombination losses. The transferred electrons in the CB of ZnO then interact with molecular oxygen adsorbed on the catalyst surface, reducing it to superoxide anion radicals.

$$e^- + O_2 \rightarrow \dot{O}_2^- \quad (3)$$

Similarly, The VB edge potential of ZnO is more positive than that of In_2O_3. This potential difference drives the photogenerated holes to transfer from the VB of ZnO to the VB of In_2O_3. The holes in the VB of In_2O_3 then directly participate in the degradation of the dye molecule. All of these highly reactive species engage in the photocatalytic degradation of dye molecules adsorbed on the photocatalyst surface to form smaller by-products [59]. Therefore, the application of indium-doped ZnO emerges as promising strategy for the effective charge separation and thereby enhancing the efficiency of photocatalytic degradation processes, particularly in the treatment of industrial dye-contaminated effluents.

The reusability of the catalyst was analyzed through multiple cycles of experiment and the efficiency for each cycle is shown in Fig. 12.

The I3ZO catalyst demonstrates excellent reusability, as established through five continuous cycles of experiments. In the first two cycles, there is no significant change in efficiency. A slight decrease in efficiency is observed in the third cycle, followed by a gradual decline in subsequent cycles. Notably, even after five cycles, the catalyst retains more than 60% of its initial efficiency, which is commendable compared to other reported catalysts [60, 61]. The observed decrease in efficiency can be attributed to the weight loss during the recovery of samples after each cycle and the partial removal of adsorbed dye molecules from the catalyst surface.

Based on Table 1, we conducted a comparative study of our prepared sample (I3ZO) against other relevant works in the literature. In-doped ZnO synthesized via the sol–gel method demonstrates superior performance in the photocatalytic degradation of RhB. It achieves a 93% removal rate at a concentration of 0.2 mM within 180 min, with a high rate

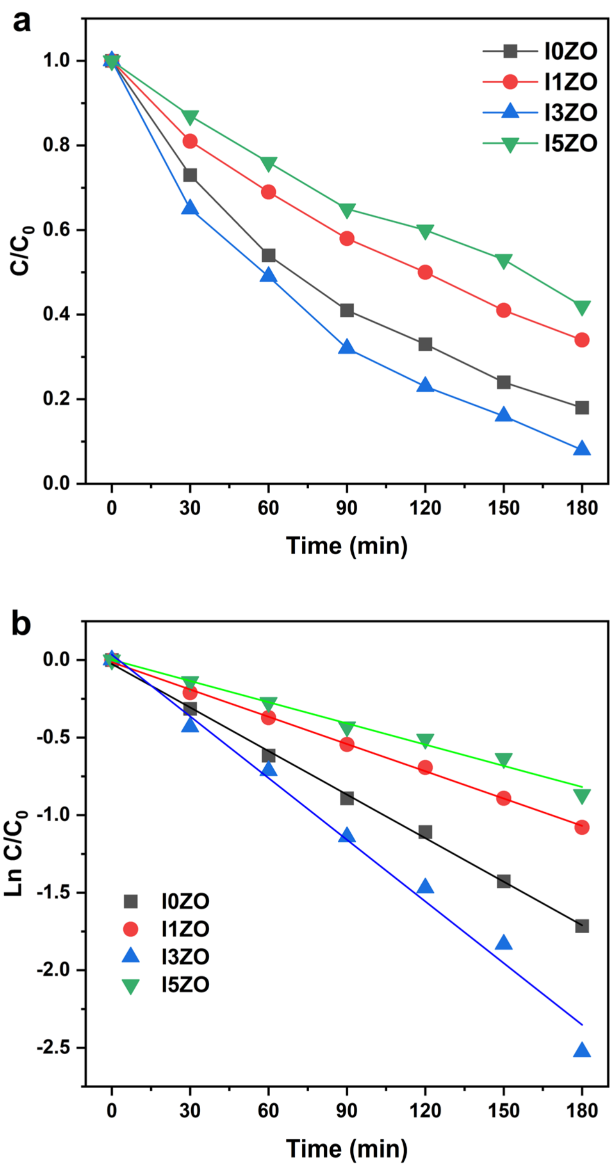

Fig. 10 **a** Time Evolution of RhB Degradation: C_t/C_0 vs. Irradiation Time Plots for All Samples, and (**b**) ln (C_t/C_0) vs. Irradiation Time Demonstrating First-Order Rate Kinetics with Linear Fitting

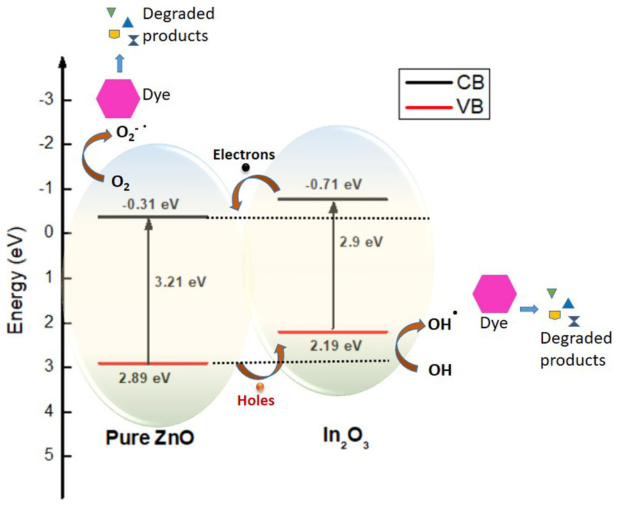

Fig. 11 Photocatalytic dye degradation mechanism

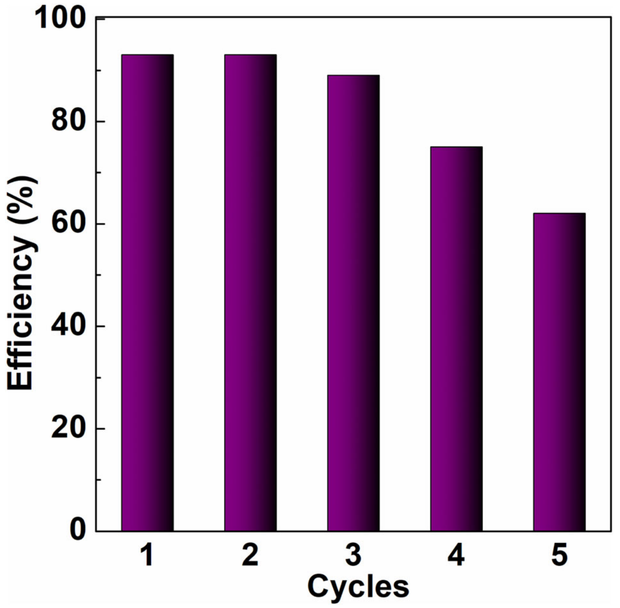

Fig. 12 Reusability of I3ZO nanopowders for mineralizing RhB

constant of 13.26×10^{-3} min^{-1} under visible light illumination. This efficiency surpasses other materials such as Fe/Cd co-doped ZnO (76% in 140 min) [60], Bi_2WO_6/FTO (94% in 240 min) [61], and Cu_2O/TiO_2 (78% in 180 min) [62]. Additionally, compared to ZnO nanoparticles synthesized via laser methods (rate constant of 2.85×10^{-3} min^{-1}) [63] and N–TiO_2/FTO (64% in 240 min) [64], In-doped ZnO not only achieves a higher removal rate but also does so more rapidly and efficiently against some materials. Furthermore, other materials such as N-ZnO/FTO (43% in 160 min) [65], ZnO/Ag (38% in 300 min) [66], and WO_3/TiO_2/FTO (58.7% in 160 min) [67] show significantly lower performance metrics. The ability of In-doped ZnO to operate effectively under visible light conditions makes it particularly advantageous for practical environmental applications. This comparative analysis clearly highlights In-doped ZnO's powerful and rapid photocatalytic capabilities, positioning it as a leading material for the photocatalytic degradation of organic pollutants.

4 Conclusion

In this work, the photocatalytic degradation of RhB under visible light irradiation by using indium-doped zinc oxide nanoparticles was investigated. Regardless of the In content ranging from 3 to 5%, indium doping induces secondary phase formation, altering ZnO microstructure, while for pure ZnO and 1% In doping, the wurtzite

Table 1 Comparative Performance of Photocatalytic Materials for Rhodamine B Degradation

Material	Synthesis	RhB concentration	Percentage removal	Time (min)	Rate constant (min^{-1})	Light illumination	References
Fe/Cd co-doped ZnO	Sol–gel	0.05 g/L	76%	140	9.16×10^{-3}	visible light	[60]
ZnO nanoparticles	Laser-Synthesized	5 mg/L	--	180	2.85×10^{-3}	UV light	[63]
Bi_2WO_6/FTO	Spray pyrolysis	30 mg/L	94%	240	$1.08 \times 10^{-4}\,s^{-1}$	visible light	[61]
N–ZnO/FTO	Electrodeposition	1 mM	43%	160	0.023	visible light	[65]
N–TiO_2/FTO	Chemical spray pyrolysis	0.5 mM	64%	240	--	UV-Visible light	[68]
N–TiO_2	Ion implantation	80 mg/L	43.2%	80	0.011	Visible light	[64]
ZnO/Ag	Chemical bath deposition	5 mg/L	38%	300	--	Visible light	[66]
WO_3/TiO_2/ FTO	Spray pyrolysis	1 mM	58.7%	160	$5.48 \times 10^{-7}\,s^{-1}$	sunlight	[67]
Bi_2WO_6/WO_3/ TiO_2	Hydrothermal	5 mg/L	66.07%	120	--	visible light	[69]
Cu_2O/TiO_2	SILAR	5 mg/L	78%	180	--	visible light	[61]
In doped ZnO	Sol–gel	0.2 mM	93%	180	13.26×10^{-3}	visible light	This work

structure is preserved. XPS analysis confirmed the presence of indium, zinc, and oxygen in the 3% In-doped ZnO sample, with no indications of metallic species, and typical spectra expected for ZnO and In_2O_3. However, with increasing the In content from 0 to 3%, we observed an enhanced surface area from 0.9 m²/g to 10.1 m²/g, which is responsible for the improvement of the photocatalytic efficiency. Therefore, In doping in ZnO nanoparticles proves to be a promising approach for sustainable photocatalysts for wastewater treatment, addressing environmental challenges posed by dye-contaminated effluents.

Supplementary information The online version contains supplementary material available at https://doi.org/10.1007/s10971-024-06471-0.

Acknowledgements The authors extend their appreciation to the Deanship of Research and Graduate Studies at King Khalid University for funding this work through Large Research Project under grant number RGP2/201/45.

Author contributions MB: Conceptualization, Methodology, Investigation, Formal analysis, Writing—original draft. KIN: Methodology & Investigation. ME: review & editing, Formal analysis. SF: XPS analysis, Review & editing. RR: Resources, Methodology. KCS: Conceptualization, Writing—review & editing. JPBS: Funding acquisition, Supervision, Review & editing.

Funding This work was also supported by: (i) the Portuguese Foundation for Science and Technology (FCT) in the framework of the Strategic Funding Contracts UIDB/04650/2020. JPBS also thanks FCT for the contract under the Institutional Call to Scientific Employment Stimulus—2021 Call (CEECINST/00018/2021). Benamara, Majdi was a Swiss Government Excellence Scholarship holder for the academic years 2023-2024 (ESKAS No. 2023.0447). The author KCS acknowledged CSIR and UGC, New Delhi, India for financial support through grant no.03/1485/23/EMR-II and No.F.4-5(59)/2014(BSR)(FRP) respectively. Open access funding provided by FCT|FCCN (b-on).

Compliance with ethical standards

Conflict of interest The authors declare no competing interests.

Publisher's note Springer Nature remains neutral with regard to jurisdictional claims in published maps and institutional affiliations.

Open Access This article is licensed under a Creative Commons Attribution 4.0 International License, which permits use, sharing, adaptation, distribution and reproduction in any medium or format, as long as you give appropriate credit to the original author(s) and the source, provide a link to the Creative Commons licence, and indicate if changes were made. The images or other third party material in this article are included in the article's Creative Commons licence, unless indicated otherwise in a credit line to the material. If material is not included in the article's Creative Commons licence and your intended use is not permitted by statutory regulation or exceeds the permitted use, you will need to obtain permission directly from the copyright holder. To view a copy of this licence, visit http://creativecommons.org/licenses/by/4.0/.

References

1. Chowdhary, P, Bharagava, RN, Mishra, S, & Khan, N (2020). Role of industries in water scarcity and its adverse effects on environment and human health. Environmental concerns and sustainable development: vol 1: air, water and energy resources. Springer, p 235–256.
2. Saravanan A, Kumar PS, Jeevanantham S, Karishma S, Tajsabreen B, Yaashikaa PR, Reshma B (2021) Effective water/wastewater treatment methodologies for toxic pollutants removal: Processes and applications towards sustainable development. Chemosphere 280:130595
3. Hemashenpagam N, Selvajeyanthi S (2023) Textile dyes and their effect on human beings. In Nanohybrid materials for treatment of textiles dyes. Springer Nature Singapore, Singapore, pp. 41–60

4. Mohan D, Shukla SP (2022) Hazardous consequences of textile mill effluents on soil and their remediation approaches. Clean Eng Technol 7:100434
5. Ahmed SF, Mofijur M, Nuzhat S, Chowdhury AT, Rafa N, Uddin MA, Show PL (2021) Recent developments in physical, biological, chemical, and hybrid treatment techniques for removing emerging contaminants from wastewater. J Hazard Mater 416:125912
6. Liu H, Wang C, Wang G (2020) Photocatalytic advanced oxidation processes for water treatment: recent advances and perspective. Chem– Asian J 15(20):3239–3253
7. Wang JL, Xu LJ (2012) Advanced oxidation processes for wastewater treatment: formation of hydroxyl radical and application. Crit Rev Environ Sci Technol 42(3):251–325
8. Kumar SG, Rao KK (2015) Zinc oxide based photocatalysis: tailoring surface-bulk structure and related interfacial charge carrier dynamics for better environmental applications. RSC Adv 5(5):3306–3351
9. Sanakousar FM, Vidyasagar CC, Jiménez-Pérez VM, Prakash K (2022) Recent progress on visible-light-driven metal and non-metal doped ZnO nanostructures for photocatalytic degradation of organic pollutants. Mater Sci Semicond Process 140:106390
10. Qiu X, Li G, Sun X, Li L, Fu X (2008) Doping effects of Co^{2+} ions on ZnO nanorods and their photocatalytic properties. Nanotechnology 19(21):215703
11. Majumdar A, Pal A (2020) Recent advancements in visible-light-assisted photocatalytic removal of aqueous pharmaceutical pollutants. Clean Technol Environ Policy 22:11–42
12. Wang Y, Wang Q, Zhan X, Wang F, Safdar M, He J (2013) Visible light driven type II heterostructures and their enhanced photocatalysis properties: a review. Nanoscale 5(18):8326–8339
13. Patil SB, Basavarajappa PS, Ganganagappa N, Jyothi MS, Raghu AV, Reddy KR (2019) Recent advances in non-metals-doped TiO_2 nanostructured photocatalysts for visible-light driven hydrogen production, CO_2 reduction and air purification. Int J Hydrog Energy 44(26):13022–13039
14. Khan H, Shah MUH (2023) Modification strategies of TiO_2 based photocatalysts for enhanced visible light activity and energy storage ability: a review. J Environ Chem Eng 11(6):111532
15. Zhang X, Peng T, Song S (2016) Recent advances in dye-sensitized semiconductor systems for photocatalytic hydrogen production. J Mater Chem A 4(7):2365–2402
16. Chatterjee D, Dasgupta S (2005) Visible light induced photocatalytic degradation of organic pollutants. J Photochem Photobiol C Photochem Rev 6(2-3):186–205
17. Ajmal A, Majeed I, Malik RN, Idriss H, Nadeem MA (2014) Principles and mechanisms of photocatalytic dye degradation on TiO_2 based photocatalysts: a comparative overview. RSC Adv 4(70):37003–37026
18. Ismail M, Akhtar K, Khan MI, Kamal T, Khan MA, M Asiri A, Khan SB (2019) Pollution, toxicity and carcinogenicity of organic dyes and their catalytic bio-remediation. Curr Pharm Des 25(34):3645–3663
19. Tahir MB, Ali S, Rizwan M (2019) A review on remediation of harmful dyes through visible light-driven WO_3 photocatalytic nanomaterials. Int J Environ Sci Technol 16:4975–4988
20. Bembibre A, Benamara M, Hjiri M, Gómez E, Alamri HR, Dhahri R, Serra A (2022) Visible-light driven sonophotocatalytic removal of tetracycline using Ca-doped ZnO nanoparticles. Chem Eng J 427:132006
21. Benamara M, Gómez E, Dhahri R, Serrà A (2021) Enhanced photocatalytic removal of cyanotoxins by Al-doped ZnO nanoparticles with visible-LED irradiation. Toxins 13(1):66
22. Ersöz E, Altintas Yildirim O (2022) Green synthesis and characterization of Ag-doped ZnO nanofibers for photodegradation of MB, RhB and MO dye molecules. J Korean Ceram Soc 59(5):655–670
23. Nguyen LT, Nguyen LT, Duong AT, Nguyen BD, Quang Hai N, Chu VH, Bach LG (2019) Preparation, characterization and photocatalytic activity of La-doped zinc oxide nanoparticles. Materials 12(8):1195
24. Habib A, Ikram M, Haider A, Ul-Hamid A, Shahzadi I, Haider J, Nabgan W (2023) Experimental and theoretical study of catalytic dye degradation and bactericidal potential of multiple phase Bi and MoS_2 doped SnO_2 quantum dots. RSC Adv 13(16):10861–10872
25. Benamara M, Zahmouli N, Kallekh A, Bouzidi S, El Mir L, Alamri HR, Valente MA (2023) Study of the magnetic properties of Mg, Gd, and Co doped maghemite (γ-Fe_2O_3) nanoparticles prepared by sol–gel. J Magn Magn Mater 569:170479
26. Benamara M, Bouzidi S, Zahmouli N, Teixeira SS, Graça MPF, Mir LE, Valente MA (2022) Electrical transport of Mg-doped maghemite (γ-Fe_2O_3) nanoparticles. Appl Phys A 128(7):624
27. Nassar KI, Tayari F, Benamara M, Teixeira SS, Graça MPF (2023) Exploring bismuth-doped polycrystalline ceramic $Ba_{0.75}Bi_{0.25}$-$Ni_{0.7}Mn_{0.3}O_3$: synthesis, structure, and electrical properties for advanced electronic applications. RSC Adv 13(34):24023–24030
28. Biesinger MC (2022) Accessing the robustness of adventitious carbon for charge referencing (correction) purposes in XPS analysis: Insights from a multi-user facility data review. Appl Surf Sci 597:153681
29. Benamara M, Massoudi J, Dahman H, Ly A, Dhahri E, Debliquy M, Lahem D (2022) Study of room temperature NO_2 sensing performances of ZnO_{1-x} ($x = 0$, 0.05, 0.10). Appl Phys A 128(1):31
30. Benamara M, Teixeira SS, Graça MPF, Valente MA, Jakka SK, Dahman H, Lahem D (2021) Study of ZnO room temperature NO_2 sensor under illumination prepared by auto-combustion. Appl Phys A 127(9):706
31. Benamara M, Ly A, Soltani S, Essid M, Dahman H, Dhahri R, Lahem D (2023) Enhanced detection of low concentration volatile organic compounds using advanced doped zinc oxide sensors. RSC Adv 13(43):30230–30242
32. Prasad KH, Kumar KDA, Mele P, Christy AJ, Gunavathy KV, Al-Buriahi MS, Alomairy S (2021) Structural, magnetic and gas sensing activity of pure and Cr doped In_2O_3 thin films grown by pulsed laser deposition. Coatings 2021 11:588
33. Benamara M, Massoudi J, Dahman H, Dhahri E, El Mir L, Ly A, Lahem D (2020) High response to sub-ppm level of NO_2 with 50% RH of ZnO sensor obtained by an auto-combustion method. J Mater Sci Mater Electron 31:14249–14260
34. Benamara M, Rivero-Antúnez P, Dahman H, Essid M, Bouzidi S, Debliquy M, El Mir L (2023) Selective and rapid detection of acetone using aluminum-doped ZnO-based sensors. J Sol-Gel Sci Technol 108(1):13–27
35. Ajmal HMS, Khan F, Nam K, Kim HY, Kim SD (2020) Ultraviolet photodetection based on high-performance Co-plus-Ni doped ZnO nanorods grown by hydrothermal method on transparent plastic substrate. Nanomaterials 10(6):1225
36. Zong Y, Sun Y, Meng S, Wang Y, Xing H, Li X, Zheng X (2019) Doping effect and oxygen defects boost room temperature ferromagnetism of Co-doped ZnO nanoparticles: experimental and theoretical studies. RSC Adv 9(40):23012–23020
37. Yu F, Hu H, Wang B, Li H, Song T, Xu B, Duan H (2019) Effects of Al doping on defect behaviors of ZnO thin film as a photocatalyst. Mater Sci Pol 37(3):437–445
38. Zhao J, Yan X, Yang Y, Huang Y, Zhang Y (2010) Raman spectra and photoluminescence properties of In-doped ZnO nanostructures. Mater Lett 64(5):569–572
39. Yu Y, Yao B, He Y, Cao B, Ma W, Chang L (2020) Oxygen defect-rich In-doped ZnO nanostructure for enhanced visible light photocatalytic activity. Mater Chem Phys 244:122672.
40. Hsu CH, Geng XP, Wu WY, Zhao MJ, Zhang XY, Huang PH, Lien SY (2020) Air annealing effect on oxygen vacancy defects in

Al-doped ZnO films grown by high-speed atmospheric atomic layer deposition. Molecules 25(21):5043.

41. Raciti R, Bahariqushchi R, Summonte C, Aydinli A, Terrasi A, Mirabella S (2017) Optical bandgap of semiconductor nanostructures: methods for experimental data analysis. J Appl Phys 121(23):234304.
42. Ekande OS, Kumar M (2021) Review on polyaniline as reductive photocatalyst for the construction of the visible light active heterojunction for the generation of reactive oxygen species. J Environ Chem Eng 9(4):105725
43. Muthukumaran S, Gopalakrishnan R (2012) Structural, FTIR and photoluminescence studies of Cu doped ZnO nanopowders by co-precipitation method. Opt Mater 34(11):1946–1953
44. Ashokkumar M, Muthukumaran S (2014) Microstructure, optical and FTIR studies of Ni, Cu co-doped ZnO nanoparticles by co-precipitation method. Opt Mater 37:671–678
45. Chung YM, Moon CS, Jung MJ, Han JG (2005) The low temperature synthesis of Al doped ZnO films on glass and polymer using magnetron co-sputtering: Working pressure effect. Surf Coat Technol 200(1-4):936–939
46. Fan JC, Goodenough JB (1977) X-ray photoemission spectroscopy studies of Sn-doped indium-oxide films. J Appl Phys 48(8):3524–3531
47. NIST X-ray Photoelectron Spectroscopy Database, NIST Standard Reference Database Number 20, National Institute of Standards and Technology, Gaithersburg MD, 20899 (2000), https://doi.org/10.18434/T4T88K
48. Moulder JF, Stickle WF, Sobol PE, Bomben KD (1992) Handbook of X-ray photoelectron spectroscopy, physical electronics, Inc., ISBN 0-9648124-1-X. Physical Electronics Division, Perkin-Elmer Corporation
49. Zhuk S, Siol S (2022) Chemical state analysis of reactively sputtered zinc vanadium nitride: the Auger parameter as a tool in materials design. Appl Surf Sci 601:154172
50. Biesinger MC, Lau LW, Gerson AR, Smart RSC (2010) Resolving surface chemical states in XPS analysis of first row transition metals, oxides and hydroxides: Sc, Ti, V, Cu and Zn. Appl Surf Sci 257(3):887–898
51. Pudukudy M, Yaakob Z (2015) Facile synthesis of quasi spherical ZnO nanoparticles with excellent photocatalytic activity. J Clust Sci 26:1187–1201
52. Khan M, Adil SF, Assal ME, Alharthi AI, Shaik MR, Kuniyil M, Siddiqui MRH (2021) Solventless mechanochemical fabrication of ZnO–$MnCO_3$/N-doped graphene nanocomposite: efficacious and recoverable catalyst for selective aerobic dehydrogenation of alcohols under alkali-free conditions. Catalysts 11(7):760
53. Kasi G, Seo J (2019) Influence of Mg doping on the structural, morphological, optical, thermal, and visible-light responsive antibacterial properties of ZnO nanoparticles synthesized via co-precipitation. Mater Sci Eng C 98:717–725
54. Wang Y, Liu X, Guo L, Shang L, Ge S, Song G, Guo Z (2021) Metal organic framework-derived C-doped ZnO/TiO_2 nanocomposite catalysts for enhanced photodegradation of Rhodamine B. J Colloid Interface Sci 599:566–576
55. Ansari SA, Ansari SG, Foaud H, Cho MH (2017) Facile and sustainable synthesis of carbon-doped ZnO nanostructures towards the superior visible light photocatalytic performance. N. J Chem 41(17):9314–9320
56. K Bhagat U, S Kshirsagar A, Gautam A, K Khanna P (2017) Low viscosity, stable TiO_2 nano-fluid for oxidative photo-degradation of methylene blue. Adv Mater Lett 8(4):506–517
57. Revathi K, Palantavida S, Vijayan BK (2019) A facile method for the synthesis of CuO-RGO nanocomposite for para nitrophenol reduction reaction. Mater Today: Proc 9:587–593
58. Murali A, Sarswat PK, Sohn HY (2019) Enhanced photocatalytic activity and photocurrent properties of plasma-synthesized indium-doped zinc oxide nanopowder. Mater Today Chem 11:60–68
59. Kuriakose S, Satpati B, Mohapatra S (2015) Highly efficient photocatalytic degradation of organic dyes by Cu doped ZnO nanostructures. Phys Chem Chem Phys 17(38):25172–25181
60. Kondamareddy KK, Bin H, Lu D, Kumar P, Dwivedi RK, Pelenovich VO, Fu D (2018) Enhanced visible light photodegradation activity of RhB/MB from aqueous solution using nanosized novel Fe-Cd co-modified ZnO. Sci Rep. 8(1):10691
61. Pedanekar RS, Madake SB, Narewadikar NA, Mohite SV, Patil AR, Kumbhar SM, Rajpure KY (2022) Photoelectrocatalytic degradation of Rhodamine B by spray deposited Bi_2WO_6 photoelectrode under solar radiation. Mater Res Bull 147:111639
62. Wang Q, Sun C, Liu Z, Tan X, Zheng S, Zhang H, Gao S (2019) Ultrasound-assisted successive ionic layer adsorption and reaction synthesis of Cu_2O cubes sensitized TiO_2 nanotube arrays for the enhanced photoelectrochemical performance. Mater Res Bull 111:277–283
63. Blažeka D, Car J, Klobučar N, Jurov A, Zavašnik J, Jagodar A, Krstulović N (2020) Photodegradation of methylene blue and rhodamine B using laser-synthesized ZnO nanoparticles. Materials 13(19):4357
64. Hou X, Liu X, Han J, Liu H, Yao J, Li D, Zhang R (2020) Enhanced photoelectrocatalytic degradation of organic pollutants using TiO_2 nanotubes implanted with nitrogen ions. J Mater Sci 55:5843–5860
65. Reis RY, Lima AE, Costa MJ, Cruz-Filho JF, Moura JP, Santos RS, Luz Jr GE (2020) Enhanced photoelectrocatalytic performance of ZnO films doped with N_2 by a facile electrochemical method. Surf Interfaces 21:100675
66. Han S, Qu W, Xu J, Wu D, Shi Z, Wen Z, Li X (2017) Chemical bath deposition of well-aligned ZnO nanorod arrays on Ag rods for photoelectrocatalytic degradation of rhodamine B. Phys Status Solidi (A) 214(9):1700059
67. Hunge YM, Yadav AA, Mahadik MA, Bulakhe RN, Shim JJ, Mathe VL, Bhosale CH (2018) Degradation of organic dyes using spray deposited nanocrystalline stratified WO_3/TiO_2 photoelectrodes under sunlight illumination. Opt Mater 76:260–270
68. Yusuf TL, Orimolade BO, Masekela D, Mamba B, Mabuba N (2022) The application of photoelectrocatalysis in the degradation of rhodamine B in aqueous solutions: A review. RSC Adv 12(40):26176–26191
69. Liu Z, Wang Q, Rong W, Jin R, Cui Y, Gao S (2018) CTAB assisted hydrothermal preparation of $Bi_2WO_6WO_3$ nanosheets on TiO_2 nanotube arrays for photoelectrocatalytic applications. Sep Purif Technol 200:191–197